InterPore JOURNAL

Original Research

3D PRINTING REACTIVE POROUS MEDIA: CALCITE PRECIPITATION KINETICS ON SURFACE FUNCTIONALIZED POLYMER FILMS AND 3D-PRINTED CORES

Harrish Kumar Senthil Kumar[1,$], Abdullah Al Nahian[2,$], Nailah Braziel[3], Zhoufan Shi[2], Madelyn Torrance[1], Vinita V. Shinde[1], Lauren E. Beckingham[2], Bryan S. Beckingham[1]

[1]Department of Chemical Engineering, Auburn University, Auburn, Alabama, USA; [2]Department of Civil & Environmental Engineering, Auburn University, Auburn, Alabama, USA; [3]Department of Biosystems Engineering, Auburn University, Auburn, Alabama, USA; [$]These two authors contributed equally to this work and should be considered co-first authors

Correspondence to:
Lauren E. Beckingham at leb0071@auburn.edu and Bryan S. Beckingham at bsb0025@auburn.edu

How to Cite:
Senthil Kumar, H. K., Nahian, A. A., Braziel, N., Shi, Z., Torrance, M., Shinde, V. V., … Beckingham, B. S. (2025). 3D Printing Reactive Porous Media: Calcite Precipitation Kinetics on Surface Functionalized Polymer Films and 3D-printed Cores. *InterPore Journal*, *2*(2), IPJ040625–7. https://doi.org/10.69631/ipj.v2i2nr71

RECEIVED: 12 Dec. 2024
ACCEPTED: 7 May 2025
PUBLISHED: 4 June 2025

ABSTRACT

Mineral precipitation reactions in porous media can change the porosity and permeability of the rock formations. Predicting the rate of reaction and impacts on formation properties is challenging due to a lack of understanding of mineral precipitation reaction kinetics and mechanisms in porous media. This is furthermore challenging due to the highly heterogeneous nature of natural porous media. Here, we aim to develop a novel experimental platform leveraging 3D printing to facilitate replicable mineral precipitation experiments in controlled, heterogenous porous media systems. This requires fundamental understanding of the kinetics of mineral precipitation on the polymer materials used to fabricate the 3D printed porous media. In this work, we manipulate (via sulfonation) material surfaces (high impact polystyrene, HIPS) to promote calcite precipitation from supersaturated solutions to inform the design of synthetic subsurface systems. Calcite precipitation on HIPS films of varied surface sulfonation is confirmed using X-ray diffraction (XRD) analysis and weight-based precipitation experiments where increased precipitation with increased surface functionalization and solution saturation index are observed. This approach is then applied to 3D-printed porous media to enhance understanding of geochemical reactions, specifically calcite precipitation. Three dimensional images of Bentheimer Sandstone are used as the basis for 3D-printed porous media samples. Two 3D-printed samples were functionalized with acid to activate the surface and promote mineral precipitation. Functionalized and unfunctionalized samples underwent calcite precipitation core flooding experiments with oversaturated calcite solutions for 96 hours. Three dimensional X-ray micro-CT imaging revealed calcite growth in functionalized samples, with a calcite volume fraction of approximately 2.6% and a substantial reduction in porosity. Unfunctionalized samples exhibited diminished calcite precipitation

and porosity changes. These findings demonstrate that reactive 3D-printed porous media can provide a versatile geochemical modeling and experimentation platform. Functionalizing 3D printed samples enhances reactivity, allowing investigations of mineral precipitation processes in complex porous media. This research highlights the potential for further exploration of 3D-printed media in various geochemical contexts.

KEYWORDS
Mineral precipitation, Surface functionalization, 3D printing, Porosity-permeability evolution, X-ray CT imaging

@2025 The Authors

This is an open access article published by InterPore under the terms of the Creative Commons Attribution-NonCommercial-NoDerivatives 4.0 International License (CC BY-NC-ND 4.0) (https://creativecommons.org/licenses/by-nc-nd/4.0/).

1. INTRODUCTION

Mineral precipitation and dissolution reactions are fundamental processes in various environmental systems, affecting natural weathering, surface and subsurface contamination, CO_2 sequestration, radioactive waste disposal, hydrothermal circulation, and biomineralization (8, 14, 20, 22, 30, 32, 74, 77, 79). These reactions alter the rock matrix by dissolving or precipitating minerals at fluid-mineral interfaces, which changes the pore shape, size, connectivity, and surface roughness (2, 7, 16, 76, 77, 101). Over time, such changes may significantly impact rock porosity and permeability, but understanding porosity-permeability evolution remains challenging due to the inherent heterogeneity of natural samples and the difficulty in replicating experiments (37, 99).

Heterogeneity in porous media, including variations in physical structure, mineral composition, and chemical reactivity, can control fluid flow, mixing, residence times, and the rate and extent of mineral reactions (3, 12, 61, 67, 73, 96). These pore-scale variations create preferential flow pathways, uneven reaction fronts, and spatially localized zones of high or low geochemical activity, which eventually could complicate the accurate prediction of reactive transport in the subsurface. Numerous studies have also shown the importance of these heterogeneities in the development of anomalous dispersion behavior and non-Fickian solute transport (13, 18, 23, 33, 34, 62, 63, 83). These studies revealed how pore-scale variability influences macroscopic transport by providing important theoretical and computational insights into dispersion mechanisms, flow channeling, and deviations from classical Fickian transport. Despite these advances, many of these approaches are limited by the assumptions of simple or constant pore geometries, the absence of reaction-induced physical changes, and the lack of controlled experimental frameworks for validation. These limitations emphasize the need for alternative experimental systems to facilitate systematic investigations into the complex coupling between heterogeneity, fluid flow, and geochemical reactions.

Additionally, the interplay between fluid flow and reactions controls mineral reactions, where reactions occur within individual pores and the larger pore network and associated impacts on permeability evolution (64, 69, 77). Ideally, one could conduct replicate experiments on the same sample to address the unpredictability in reaction rates and permeability evolution caused by natural heterogeneities. However, this is generally not feasible as reactions result in irreversible changes to the sample, and even replicate experiments on samples from the same location have shown inconsistent results in determining porosity-permeability evolution (52).

Furthermore, pore network modeling (PNM) is a well-established and computationally efficient method for studying fluid flow, solute transport, geochemical reactions, and structural evolution in porous media. Pore network modeling allows researchers to evaluate how pore-scale heterogeneity, such as pore and throat size variations, connectivity, and mineral distribution, affects permeability evolution and localized reactions under different flow and geochemical conditions. Numerous studies have utilized PNM to

provide valuable insights into how spatially variable dissolution and precipitation influence the relationship between porosity and permeability (17, 84, 89). These studies have shown that changes in permeability are significantly influenced by the location and geometry of minerals rather than porosity alone.

The use of PNM has been helpful in capturing phenomena such as wormhole formation and channel competition (47, 82), as well as understanding the impact of pore-throat distributions, coordination number and anisotropy on flow localization and reactivity (10, 36, 97). Additionally, PNM provides insights into scaling behaviors and the upscaling of geochemical reaction and adsorption rates from pore to continuum scales (53, 58, 59, 80), and it has helped quantify discrepancies between laboratory and field-scale predictions under transport-limited conditions (70). Recent advancements have incorporated pre-asymptotic shear dispersion effects into PNM frameworks, enhancing the simulation of non-Fickian transport and local mass transfer (34, 63).

Pore network modeling is limited by assuming idealized geometries (e.g., spherical pores, cylindrical throats), constant topology, and the assumption of uniformly reactive or inert pores (10, 59, 76, 97). These limitations restrict its ability to resolve pore-scale structural evolution and reaction heterogeneity. In contrast, high-resolution direct numerical simulations (DNS), such as Lattice Boltzmann or finite volume methods, can capture realistic geometries derived from micro-computed tomography (CT) imaging (93). However, they are computationally intensive and often confined to small domains. Considering all these limitations, 3D printing presents a promising experimental complement to PNM, allowing the design of porous media with modifying heterogeneity and reactive properties. This approach can help validate model predictions and investigate dynamic flow-reaction coupling under well-controlled conditions.

Three dimensional printing shows significant potential for replicating the heterogeneous properties of natural rock samples, advancing the study of porous media. Researchers have utilized 3D printing to explore the hydraulic properties of soils, analyze changes in flow characteristics due to evolving pore networks, and investigate rock mechanics (55, 57, 78, 85, 86, 88). Song et al (88) assessed the ability of 3D printing to replicate the intrinsic bulk properties of natural porous rocks, while Kong et al (55) demonstrated microstructural similarity between 3D-printed and natural Berea sandstone. Recent advancements include Oskolkov et al (78), who used fused filament fabrication (FFF) 3D printing with CT-guided designs to replicate sandstone cores, precisely tuning porosity and permeability through material flow and overlap adjustments. Similarly, Lee et al (57) employed material jetting 3D printing to fabricate high-resolution sandstone micromodels, validated using 3D X-ray micro-CT and microfluidic studies, confirming their accuracy and reproducibility. These studies collectively emphasize the potential of 3D-printed rocks to replicate natural samples, facilitating a deeper understanding of rock properties and the influence of pore structure variations on macroscopic behavior.

Despite its potential, the use of 3D printing to understand mineral reactions and porosity-permeability evolution in porous media remains limited. The goal is for 3D printers to quickly produce multiple replicate samples with identical pore structures based on 3D X-ray micro-CT images of real porous media samples. This would offer significant advantages over natural geological samples, which cannot be identical even if they come from homogeneous formations. It should be noted, however, that porous media structures often must be substantially magnified so that features are larger than the 3D printer resolution.

Geochemically reactive fabricated porous media have been explored to understand geochemical reactions in natural rocks (9, 85). Such studies considered the addition of a reactive mineral phase, calcite, to the filament or printing resin, but faced challenges in controlling the distribution of reactive particles within printed structures (9, 85). This study aimed to understand the feasibility of creating reactive 3D-printed porous media via surface functionalization, and subsequently, using these samples to enhance understanding of mineral reaction rates in porous media. Towards this goal, the viability of surface functionalization of polymer films to enhance calcite precipitation was first explored, and the developed surface functionalization method was then applied to complex 3D printed porous media samples.

The mineral investigated in this study was calcium carbonate ($CaCO_3$), one of the most abundant minerals on earth. It is commonly found in limestones and sandstones and occurs widely across the globe (6). Understanding calcium carbonate precipitation and calcium carbonate mineral growth kinetics is critical for predicting mineral weathering and geologic CO_2 sequestration (15, 35, 46, 102). Calcium carbonate is also used in a wide range of additional applications where understanding calcite precipitation kinetics is necessary. These include its role as the primary component in cement production, as an abrasive in dental and surface polishing products, in agricultural soil treatments to enhance crop yields, and in calcium looping processes for CO_2 sequestration. There have been recent developments in using polymers as biomaterial substitutes for joint implants, where understanding calcium carbonate deposition is vital for decreasing the chance of implant failures and other difficulties (27, 48, 95, 98). A recent report also found that the precipitation of calcium carbonate on microplastics when water is boiled can remove microplastics from drinking water due to the subsequent sedimentation of the precipitates (100).

Crystal growth mechanisms are classified into two types, homogenous crystallization and heterogenous crystallization. Heterogenous nucleation is the process of growing a crystal on the surface of another solid (heterogenous nucleation crystallization), whereas homogenous nucleation crystallization takes place in the absence of a second phase (1, 11, 19, 60, 65). Crystallization typically takes place either due to supersaturation or supercooling of the liquid phase. Supersaturation is a state where the amount of dissolved solute (e.g., $CaCO_3$) in a solvent (e.g., water) is greater than the equilibrium solubility. This makes the system thermodynamically out of equilibrium, and the system tries to return to a stable thermodynamic state by nucleating and growing crystals of the dissolved solute.

Calcite growth and precipitation equilibria is described as (5, 38, 49, 50) (**Eq. 1**):

$$CO_3^{2-} + Ca^{2+} \leftrightarrow CaCO_3\ (s) \quad (1)$$

where calcium cations (Ca^{2+}) and carbonate anions (CO_3^{2-}) are present in the solution and combine to form solid calcium carbonate or calcite. Prior investigations of calcite crystallization have found that calcite nucleation and growth kinetics depend on the saturation index of the solution, pressure, nature of the reservoir rock, and flow conditions (4, 5, 29, 40, 49, 51, 66, 68, 71, 90).

At constant temperature, the saturation index (SI) plays a key role in crystal nucleation as given by **Equation 2**:

$$SI = \frac{\alpha_{Ca}^{2+}\alpha_{CO3}^{2-}}{K_{sp,CaCO3}^{\circ}} \quad (2)$$

where α_i^j is the activity of the ion i with charge j, and $K_{sp,CaCO3}^{\circ}$ is the thermodynamic solubility product of the crystal at ambient conditions (50). Nucleation rate is dependent on the saturation index, where for an increasing saturation index, the rate of nuclei formation is higher than the rate of crystal growth, resulting in the formation of elongated crystals. Whereas for a lower saturation index, the interactions between the solution ions and the solvent (usually water) are reduced, resulting in the formation of platy crystals (26). For systems where there is flow, a higher volumetric flow rate of the supersaturated solution results in slower crystal formation (lower crystal yield over time) (87, 92). The above-mentioned factors of saturation index, pressure exerted by the formed crystal, and volumetric flow rates all play key roles in the precipitation behavior, and are thereby important factors to investigate in order to better understand and/or predict precipitation behavior in both simple single mineral systems and more complex natural systems.

To precipitate and grow minerals on polymeric films, the energy barrier for mineral crystal growth must be overcome. In many cases, this requires surface modification to manipulate the surface energy associated with the polymeric surface (usually increase the surface energy). Prior studies of mineral growth on polymeric surfaces have included surface functionalization of poly(lactide-co-glycolide) towards mimicking the growth of bonelike mineral for understanding biomineralization (72) and apatite-like mineral growth on high molecular weight polyethylene and polyurethane (PU) foams where the surface was modified by a calcium based precursor (81). A kinetic analysis of how polymers with different

functional groups influence the inhibition of mineral nucleation in gypsum was performed and reveals that polymers significantly affect the rate of gypsum crystal formation by altering crystallization process based on different functional groups in the polymers. They also observed that the role of polymers in the nucleation process, as interpreted through classical nucleation theory, is inconsistent and fails to provide a physically meaningful explanation for the observed effects (28, 75). While there is existing literature on the induced crystallization kinetics caused by the addition of polymers, studies focusing on using polymer surfaces and modified polymeric surfaces to promote crystal growth are limited and require further investigation.

Here, the impact of surface functionalization via sulfonation on the growth of calcite on high impact polystyrene (HIPS) films was investigated. High impact polystyrene is a common commercial thermoplastic polymer material that is easy to process and offers good mechanical properties (rigid, durable, stable environmentally, etc.) that can be readily sulfonated with sulfuric acid at ambient temperatures (42, 43, 94). In this work, HIPS films were sulfonated to varying degrees and used in flow-through calcite precipitation experiments where precipitation kinetics were discerned by measuring the amount of calcite precipitation onto the films over time. In addition to the degree of sulfonation, the impact of saturation index was investigated for four different saturation indexes, towards better understanding of mineral growth kinetics over surface functionalized HIPS. Next, porous media samples based on 3D X-ray CT images of Bentheimer sandstone were printed, functionalized with acid, and used in calcite precipitation core flood experiments. Three dimensional X-ray micro-CT images of reacted samples were collected and used to observe calcite precipitation and discern changes in porosity. Results from functionalized and unfunctionalized core samples were compared to evaluate the potential of surface functionalization to support fabrication of 3D printed reactive porous media.

2. MATERIALS AND METHODS

2.1. Materials

High impact polystyrene (HIPS) pellets and polylactic acid (PLA) pellets[a] were used to prepare films for precipitation experiments. Sulfuric acid (98% pure)[b] was used for the functionalization of the HIPS films. Sodium bicarbonate and calcium chloride salts[c] were used for preparing the solutions. Chloroform ($CHCl_3$)[c] was used for the NMR spectroscopy. Peristaltic pumps[d] were used for the flow experiments. UV Tough Resin[e] was used for 3D printing the custom experimental flow chamber. A Bentheimer sandstone from the Valaginian formation was selected for printing 3D porous media. The sample was a ½ inch diameter x 1 inch length core sample predominantly composed of quartz with porosity and permeability of 23 to 26 % and 1500 to 3500 mD[f], respectively.

2.2. 2D HIPS film surface functionalization

The HIPS pellets were fabricated into thin 2D films of uniform shape by compression molding on a heated press[g] at 180°C. After cooling, the films were immersed in individual sulfuric acid baths (98% pure sulfuric acid diluted to 75% acid concentration with distilled water) at room temperature for varying time intervals. The films were removed and washed with deionized (DI) water and analyzed to confirm the presence of sulfuric acid groups using both Fourier-transform infrared (FTIR) spectroscopy and Proton nuclear magnetic resonance (^{1}H-NMR) spectroscopy. The HIPS films that were not exposed to the sulfuric acid bath were effectively a control for the impact of surface functionalization on subsequent

[a] *3DXTech: https://www.3dxtech.com/*

[b] *Fisher Scientific: https://www.thermofisher.com/*

[c] *VWR BDH Chemicals: https://www.vwr.com/bdh*

[d] *INTLLAB BT100: https://www.carousell.sg/p/intllab-bt100-variable-speed-peristaltic-pump-with-pump-head-yz15-flow-rate-0-06-360-ml-min-0-1-100rpm-with-2-meter-17-tubing-c0035-1236302983/*

[e] *Anycubic: https://www.anycubic.com/*

[f] *Kocurek Industries INC.: https://kocurekindustries.com/*

[g] *Carver (Model 4389): https://carverpress.com/presses-accessories/bench-top-manual-press/heated/*

precipitation experiments. The film surface was also examined before and after acid treatment by optical microscopy for surface degradation, **Figure S1** in the **Supplementary Material** (available online).

2.3. Functionalized 2D film characterization

Fourier-transform infrared spectroscopy was performed on the pressed films (both control HIPS film and functionalized HIPS films) using a spectrometer[h] equipped with attenuated total reflection (ATR) by placing the films in contact with the ATR assembly and acquiring the spectra. Proton nuclear magnetic resonance spectroscopy was performed by first dissolving the untreated HIPS films (control sample) and acid-treated HIPS samples in chloroform in separate NMR tubes, and once fully dissolved, ^{1}H-NMR spectra were collected on a Benchtop Spectrophotometer[i]. A sessile drop goniometer was utilized to measure the contact angle of the functionalized 2D HIPS films in triplicate. Each film was subjected to a standard 10-second automated contact angle goniometer experiment, which determined the mean contact angle with the averages and standard deviation reported.

2.4. 2D Film Flow Precipitation Experiments

A custom-made flow chamber was designed, and 3D printed to perform the flow experiments, schematic and photo are shown in **Figure S2** (**Supplementary Material**, available online). The functionalized 2D HIPS films were placed inside the 3D printed flow chamber. Freshly prepared calcite stock solutions were mixed in equal volumes producing the desired saturation index of 3.15. The solution was then passed through the 2D film holder with the functionalized films using a peristaltic pump[d] at a set flowrate and the effluent was collected at the other side. A series of flow precipitation experiments were then conducted on surface functionalized films. A saturation index (SI) of 3.15 was chosen. The flow rate was kept constant and as low as possible in our system (0.9 ± 0.1 ml/min for all experiments) to reduce impacts on the precipitated surface crystals due to bulk fluid flowing. The experimental design was conducted for non-functionalized films, as well as films functionalized for 24, 48, 96, 168, and 240 hours with precipitation times of 1, 2, 4, 8, and 24 hours. All experiments were performed in at least triplicate on independently prepared films. The weight of each 2D film was noted prior to the experiment. After precipitation, the 2D films were carefully patted dry, and their final weight was measured. The difference between the initial and the final weights represents the amount of mineral precipitation on the functionalized film.

2.5. X-ray Diffraction Analysis

X-ray diffraction (XRD) was performed on the precipitated mineral phase using a Proto manufacturing AXRD powder diffraction system with Cu K_α radiation (λ = 1.5418 Å). The precipitated calcite on the film surface was scraped off the film and loaded into the XRD as a powder. Additional XRD analyses, provided in the **Supplementary Material** (available online), were performed on both control and functionalized HIPS films by mounting the films directly onto the XRD stage. Samples were scanned at a rate of 2.4°/min ($\Delta 2\theta$ = 0.0139°, with a dwell time = 5 s) from 15° to 40 ° (2θ) at 30 mA and 40 kV.

2.6. Fabrication of 3D Printed Porous Media

A 3D X-ray micro-CT image of the Bentheimer sample was acquired using a 3D X-ray microscope[j] at 10.76 microns (**Fig. 1**). Three dimensional X-ray micro-CT images were manually segmented into grain and pore voxels using ImageJ[k]. Prior to segmentation, images were filtered by the non-local means denoising filter (24) from the plugin in ImageJ to remove noise. Mesh files for 3D models were generated in Dragonfly[l] by selecting sub-regions from the segmented images of the sandstone sample. The mesh was then converted to a stereolithography (.stl) file to serve as the 3D printing mesh (**Fig. 1**). A cylindrical

[h] *Thermo Scientific Nicolet 6700 FTIR: https://www.thermofisher.com/de/de/home/industrial/spectroscopy-elemental-isotope-analysis/molecular-spectroscopy/fourier-transform-infrared-spectroscopy.html*

[i] *Oxford Instruments 60 MHz (1.4 T): https://nmr.oxinst.com/assets/uploads/MagRes/Brochures/MR_Pulsar_Brochure_8PP_2019_Web_March_2019.pdf*

[j] *ZEISS Xradia 620 Versa: https://www.zeiss.com/microscopy/en/products/x-ray-microscopy/versaxrm.html*

[k] *ImageJ: https://imagej.net/ij/*

[l] *A 3D visualization and analysis application by Object Research Systems Inc.: https://dragonfly.comet.tech/*

region of interest was selected from the mesh files of the sample and cropped to a uniform size. The cropped region of interest was 5 x 5 x 7 mm. The final mesh was then enlarged to such a magnification that the final size of printed samples was 22 x 22 x 31.5 mm.

Samples were fabricated using high impact polystyrene (HIPS) 1.75 mm diameter filament[m] using a 3D printer[n] (**Fig. 1**). The extrusion temperature was set to 240°C. For the print bed, the temperature was maintained at 115°C for the first layer and 110°C for the remaining layers. The infill density was set at 100% with a rectilinear fill pattern, and the print speed was 50%. Prior to 3D printing, a thin layer of Kores glue was applied to the print bed to ensure sufficient adhesion and prevent warpage of the initial layers.

Surface functionalization was employed on 3D-printed samples through sulfonation with sulfuric acid to enhance calcite precipitation. This process introduces sulfonic acid groups onto the HIPS film surface, increasing surface hydrophilicity and lowering surface energy, which promotes the seeding and growth of calcite crystals. An 11 M sulfuric acid solution (98% pure sulfuric acid diluted with distilled water at 75:25 volume%) was used for sulfonation at room temperature for seven days. These conditions were based on the 2D film experiments for calcite precipitation on functionalized films described above.

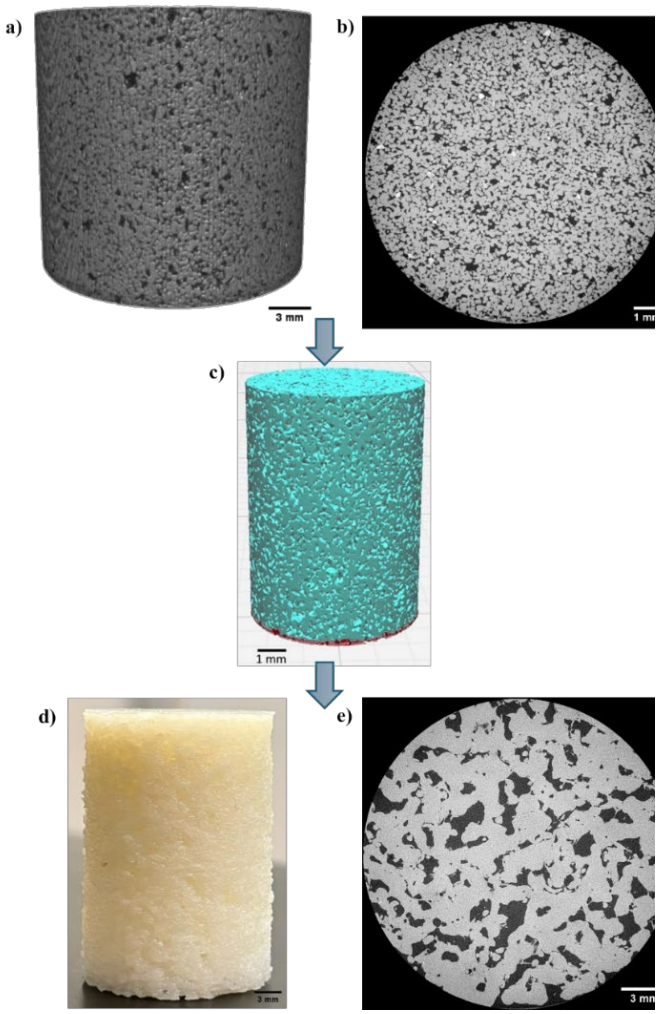


Figure 1 a) 3D X-ray micro-CT image of Bentheimer sandstone; **b)** 3D X-ray micro-CT image slice of Bentheimer sandstone; **c)** cropped and meshed image of Bentheimer sandstone; **d)** 3D X-ray micro-CT image of 3D-printed sample and **e)** 3D X-ray micro-CT image slice of the 3D-printed sample.

2.7. Calcite Precipitation Experiments

A custom core flooding experimental setup (**Fig. 2**) was used to carry out precipitation experiments in 3D-printed samples. A resin-manufactured core holder was designed and printed to contain the 3D-printed core sample. The core holder was printed in two parts to facilitate the insertion of the porous media. Before placing the core sample inside the core holder, a heat shrink tube was wrapped around the sample to minimize the gap between the sample and the core holder, encouraging the fluids to flow exclusively through the sample. Despite this, some space remained between the heat-shrink-covered sample and the core holder due to the rough surface of the sample. To address this, an epoxy adhesive (a mixture of epoxy resin and hardener) was used to fill the remaining gaps, preventing free flow through the surrounding void areas and securing the two parts of the core holder together. During the flow experiments, a needle valve was used downstream to create back pressure (~ 3 psi), which helped to saturate the samples with fluid by removing trapped air from the porous media.

[m] *Gizmodorks, 3DXTech: https://gizmodorks.com/?srsltid=AfmBOooUoOeJP25UML6WroLgLWvIqXKrxMWA4IGcc1-YNBwss6DX9C14*

[n] *Prusa Research, MK3S+ Prusa FFF: https://www.prusa3d.com/de/kategorie/original-prusa-i3-mk3s-2/*

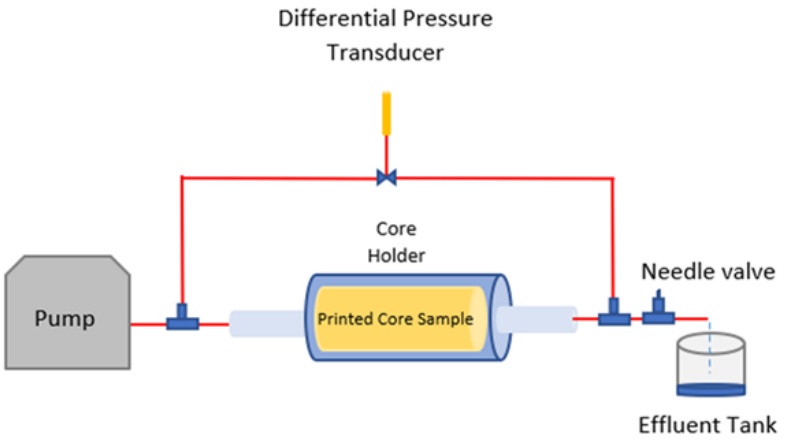


Figure 2: Core-flooding experimental setup for the calcite precipitation experiments.

Four replicated precipitation experiments were conducted using two unfunctionalized samples (U-1 and U-2) and two functionalized samples (F-1 and F-2). Fluids were injected using a variable-speed peristaltic pump. Samples were first saturated with water before injecting a calcite supersaturated solution. A solution comprised of 0.04 M $NaHCO_3$ and 0.02 M $CaCl_2$ was used to promote calcite growth in the sample. The calcite solution was injected at a flow rate of ~1.3±0.04 ml/min, and the experiments were run for 96 hours at room temperature and pressure. The saturation index of the solution was 3.15, suggesting the solution is oversaturated with respect to calcite. This saturation index (SI) was selected from 2D film calcite precipitation experiments to promote rapid calcite precipitation within a manageable experimental timeframe. Additional experimental data under identical experimental conditions (such as functionalization time and porosity), have been provided in the supplementary information **Table S1** in the **Supplementary Material** (available online).

Three dimensional X-ray micro-CT images of the reacted samples were taken at the end of the precipitation experiments to determine the porosity changes and observe the calcite growth. Image acquisition properties are given in **Table 1**. Images were processed by selecting a region of interest and cropping the associated selection from the 3D X-ray micro-CT images of the reacted samples using ImageJ. The non-local means denoising filter from the plugin in ImageJ was used to filter the images and remove noise. Images were then manually segmented into grain, water, pore, and calcite voxels using ImageJ. Segmented images containing only grain, water, pore, and calcite voxels were saved. Then, these individual images were combined using a MATLAB code. After the segmentation, there was still some noise evident from the image segmentation process. This was corrected by identifying small,

Table 1: 3D X-ray CT image acquisition properties for the functionalized (F-1, F-2) and unfunctionalized (U-1, U-2) core sample experiments.

Sample	FOV (µm)	Voxel size (µm)	Scanning voltage	Exposure time (s)	Number of projections
Bentheimer	11080 x 11080	10.76	70	1.5	3200
F-1	23552 x 23552	23	50	2.5	3200
F-2	21508 x 21508	21	50	4	3200
U-1	24091 x 24091	23.53	50	4	3200
U-2	24090 x 24090	23.53	50	4	3200

connected voxel regions with **bwconncomp** in MATLAB and then flipping the labels to agree with the surrounding bulk phase.

Calcite precipitation and the evolution of the printed sample properties were determined from quantitative image processing. Images were analyzed to determine the porosity before and after the core-flooding experiments, connected and unconnected porosity, and calcite volume fractions. The connected was identified using a burning algorithm to identify connected pore voxels and unconnected porosity inferred by comparison with the total porosity. The percentage of calcite and sample porosity were calculated by voxel counting using MATLAB, and the distribution of calcite throughout the porous media was considered. The percentage of calcite was computed using **Equation 3**:

$$\phi_{calcite} = \frac{N_{calcite}}{N_{total}} \quad (3)$$

where $\phi_{calcite}$ is the percentage of the calcite (%), $N_{calcite}$ is the total number of the calcite voxels in the image and N_{total} is the total number of the voxels in the image. Then, the mass of the precipitated calcite was determined by using **Equations 4** and **5**:

$$V_{calcite} = \phi_{calcite} \text{ x } V_{total} \quad (4)$$

$$M_{calcite} = V_{calcite} \text{ x } \rho_{calcite} \quad (5)$$

where $V_{calcite}$ is the total volume of the calcite (cm^3), V_{total} is total volume of the porous media (cm^3), $M_{calcite}$ is the mass of the calcite (g) and $\rho_{calcite}$ is the bulk density of the calcite ($2.71 gcm^{-3}$).

3. RESULTS AND DISCUSSION

To understand calcite precipitation onto polymer surfaces, the following sections detail our investigation of the impact of polymer surface functionalization and solution saturation index on calcite precipitation kinetics. First, the results of polymer film characterization before and after surface functionalization with sulfuric acid for varied times are presented, followed by the results of calcite precipitation experiments. Subsequently, 3D printed cores were fabricated from X-ray CT images of a real Bentheimer sandstone sample, and the impact of surface functionalization on calcite precipitation was evaluated via core-flooding experiments and X-ray CT image analysis.

3.1. Surface functionalization of 2D HIPS films

Here in this section, we have investigated surface functionalization of HIPS and characterized the change in surface energy with functionalization time via contact angle measurements. Contact angles give a relative measure of surface energy. A higher contact angle represents a more hydrophobic surface and a lower surface energy, whereas a lower contact angle represents a more hydrophilic surface and a higher surface energy. Here, we manipulate the surface energy through surface functionalization with sulfuric acid. Sulfonation of HIPS films was caried out using sulfuric acid (98% purity), diluted to a 75:25 volume ratio with distilled water. Films were treated for varying time intervals to produce surfaces with differing concentrations of sulfonic acid groups, which increase with longer sulfonation times. This surface modification was intended to enhance polymer hydrophilicity (through increased surface charge) and promote calcite nucleation on the polymer surface. First, whether the acid treatment degraded the polymer film or substantially altered the surface character was investigated. Following acid treatment, films were weighed and there was no detectable change in film weight. The film surfaces were also examined via optical microscopy (**Fig. S1**, **Supplemtary Material**, available online), where no change in

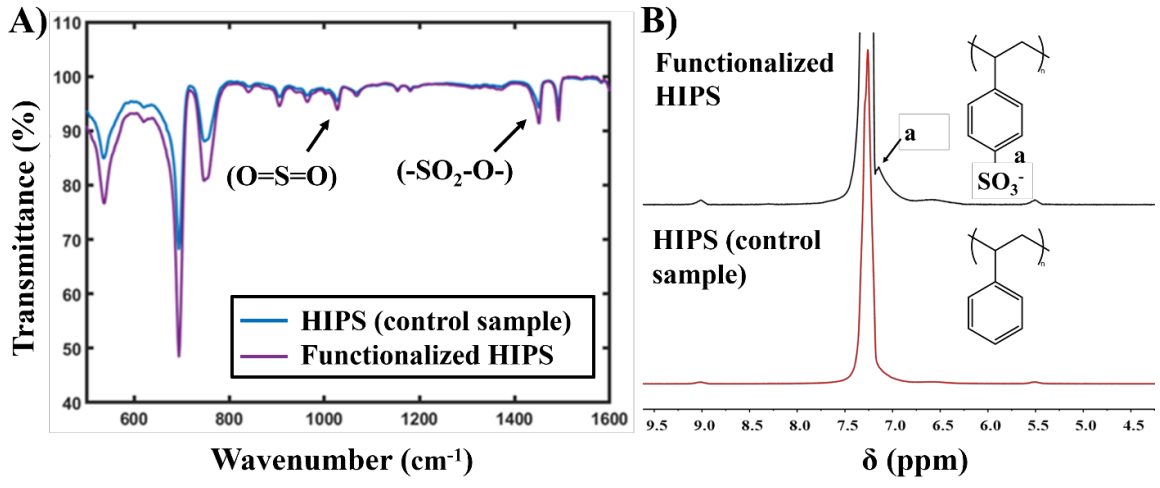


Figure 3: A) FTIR spectrum of HIPS film (blue) and acid treated HIPS film (violet), **B)** NMR spectrum of HIPS (red), and acid treated HIPS (green).

the surface character was observed. Acid treated films (2 days functionalized) were characterized using ATR-FTIR and ^{1}H-NMR spectroscopy to confirm the presence of sulfonic acid groups. The FTIR spectra showed a weak absorption of the sulfonic acid group (O=S=O) and stretching vibration of SO_2 (-SO_2-O) around 1023 cm^{-1} and 1175 cm^{-1} respectively (**Fig. 3A**). These peaks in the FTIR spectra are due to the partial sulfonation of the HIPS films on sulfuric acid treatment. The ^{1}H-NMR spectra shows the sulfonated HIPS shoulder peak at 7.07 ppm which confirms the partial sulfonation of the benzene ring in HIPS owing to surface functionalization (**Fig. 3B**) (87).

Indeed, as shown in **Figure 4**, the surface energy of the HIPS films increases with increasing surface functionalization. The change in surface charge was analyzed by performing contact angle measurements and the increase in surface functionalization was observed with an increase in time given for functionalization (**Fig. 4**). The contact angle decreases with an increase in functionalization time and

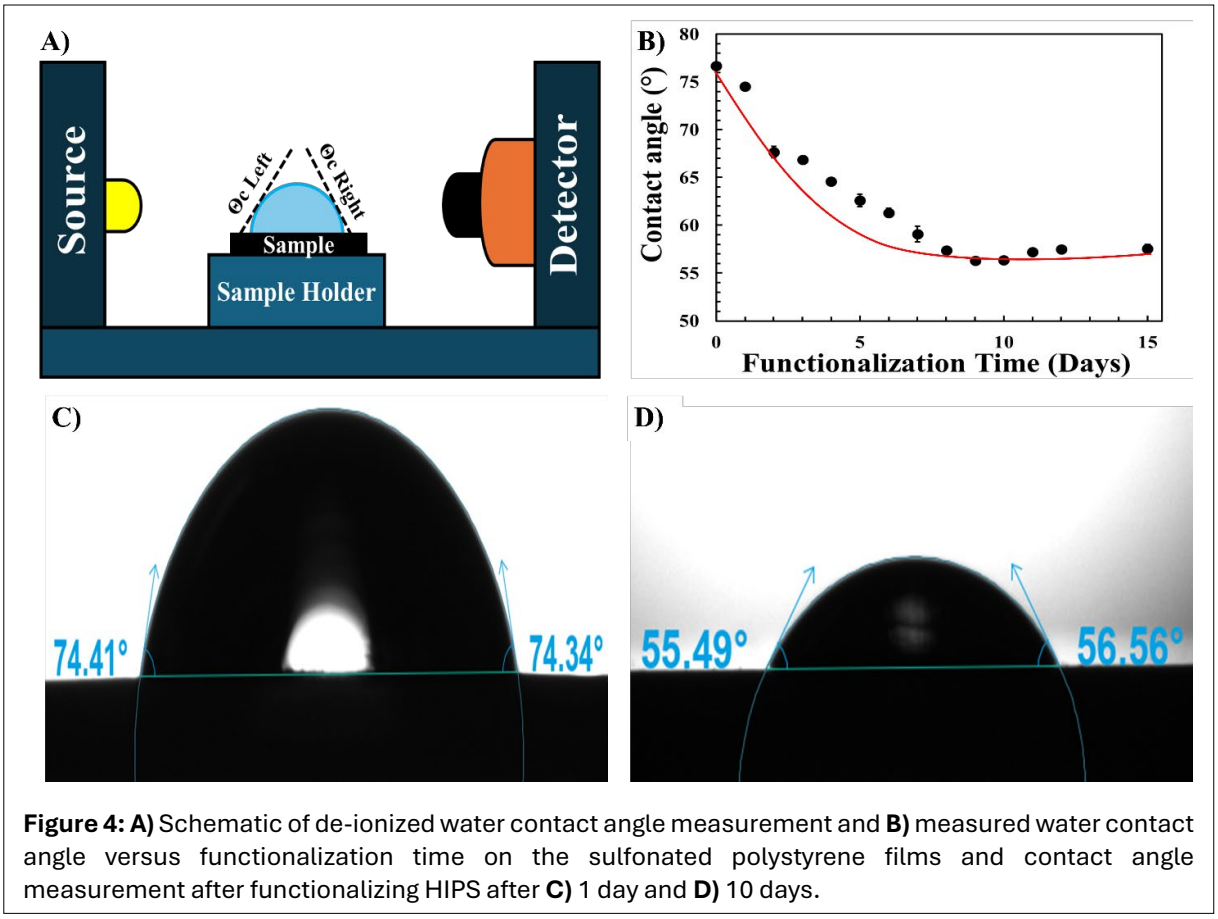


Figure 4: A) Schematic of de-ionized water contact angle measurement and **B)** measured water contact angle versus functionalization time on the sulfonated polystyrene films and contact angle measurement after functionalizing HIPS after **C)** 1 day and **D)** 10 days.

reaches a plateau after 9 days, indicating maximum threshold for functionalization. Thus, we limited calcite precipitation experiments, as discussed in the next section, to 10 days of surface functionalization.

To better understand the impact of surface functionalization of the 2D films, a relation based on Young's equation was used as follows (39, 44, 45) (**Eq. 6**),

$$\gamma_{sv} = \gamma_{sl} + \gamma_{lv} cos\theta \quad (6)$$

where, γ_{sv} represents the surface energy of the solid, γ_{sl} represents the interfacial tension between the liquid and the solid, γ_{lv} represents the surface tension of the liquid (deionized water) and θ is the contact angle of the liquid on the solid surface (polymer film). The reported surface energies of calcite ~57 mJ/m^2 - 58 mJ/m^2 (25) and the non-functionalized films had no measurable precipitation due lower surface energy (58.47 mJ/m^2). The unfunctionalized HIPS films need to overcome the minimum energy barrier required for calcite to nucleate over the substrate. With an increase in surface functionalization, surface energy increases and thus helps the calcite mineral to nucleate and precipitate over the 2D reactive surface. Surface energies corresponding to the measured contact angles were calculated using Young's

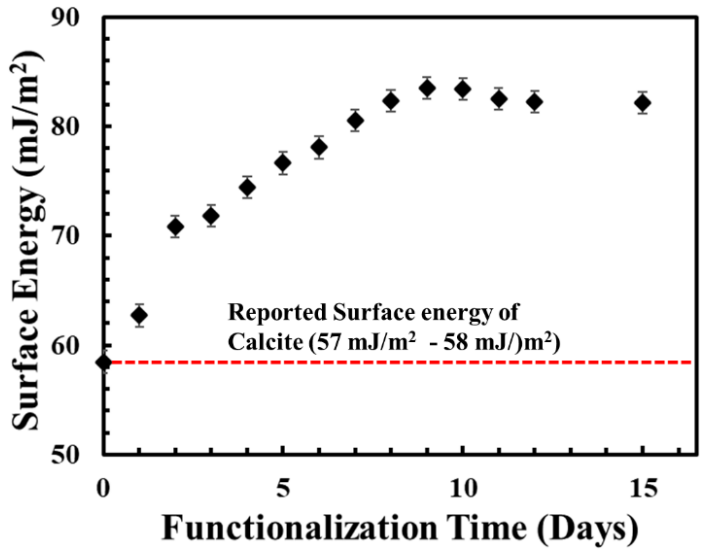


Figure 5: Surface energies of HIPS films over time given for functionalization. The red dash line indicates the HIPS control sample value (0 day functionalized).

equation. The results (**Fig. 5**) showed that surface energy (mJ/m²) increased with longer functionalization times, eventually plateauing after 9–10 days. Notably, the surface energy of the unfunctionalized HIPS film was close to the threshold required for calcite precipitation, whereas the functionalized HIPS films exhibited significantly higher surface energies, easily surpassing the energy barrier necessary for precipitation. Further experiments related to these findings are detailed in Section 3.2.

3.2. Calcite growth on surface functionalized 2D films

The 2D films, both unfunctionalized and functionalized for different durations, were subjected to calcite precipitation reactions by flowing calcium carbonate solutions across them in a custom-built flow chamber (**Fig. S2**, available online). A saturation index (SI) of 3.15 was selected to ensure precipitation occurred within our desired experimental time frame based off of literature reports for which precipitation occurs over longer time frames for a saturation index of 1.42 (77). Thus, the increased SI of 3.15 was chosen to promote precipitation in shorter experimental times.

X-ray diffraction (XRD) was performed on the functionalized HIPS films before and after calcite precipitation, and the results compared to the XRD pattern for bulk calcite powder as a reference sample (**Fig. 6A**). Bulk calcite shows a characteristic calcite peak at 29.5 (2θ) and this characteristic calcite peak is present for the precipitated calcite scraped off the functionalized HIPS films after calcite precipitation experiments confirming the precipitated mineral to be calcite (3). This is an important confirmation as calcium carbonate can also precipitate into two other polymorphs (aragonite and vaterite). Note, this calcite peak is not observed in the spectra for either the control or functionalized HIPS films prior to the precipitation experiments (**Fig. S4** in the **Supplementary Material**, available online). Scanning electron microscopy (SEM) was also performed to examine the crystal morphology (**Fig. 6B**) revealing that the

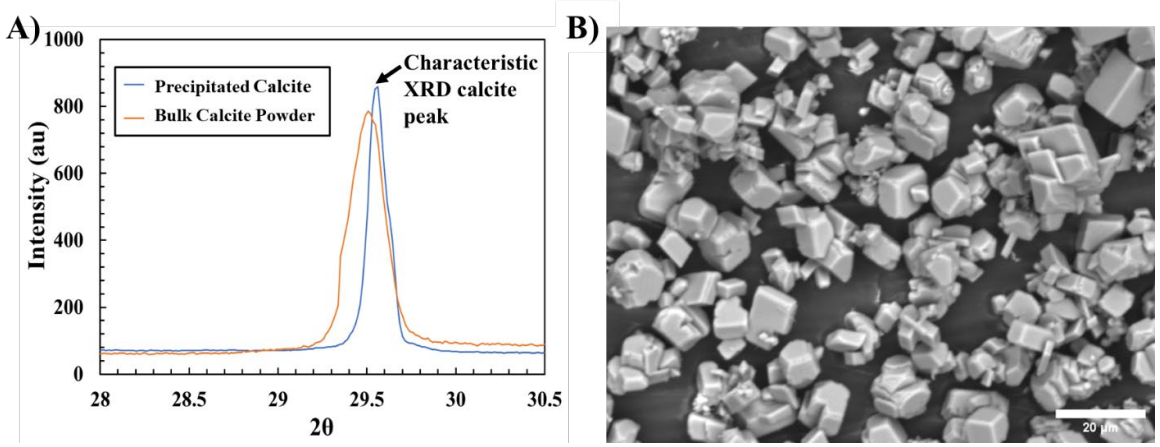


Figure 6: A) X-ray diffraction spectra of bulk calcite powder (reference) and representative XRD spectra of scraped off calcite grown on a 2 day functionalized HIPS film. **B)** SEM image of a surface functionalized 2D HIPS film (10 days) depicting calcite precipitation.

precipitated calcite crystals exhibited the characteristic rhombohedral-like shapes expected for calcite (21, 91).

As shown in **Figure 7**, the amount of calcite precipitate on the 2D films increased with increasing functionalization time. Note that precipitation on the unfunctionalized film (yellow square, lower right) had no measurable calcite precipitate after 24 hours. Given the increase in precipitation with functionalization time, we conclude that surface modification of the 2D HIPS films via sulfonation promotes calcite precipitation. The precipitation of calcite over the functionalized films is due to the presence of sulfuric acid moieties after surface functionalization. These sulfonic acid moieties act as seeding sites for calcite to precipitate. Further, increasing the degree of surface sulfonation, and thereby increasing the surface energy, promotes increasing calcite precipitation, likely by reducing the energy barrier for calcite crystal nucleation and growth.

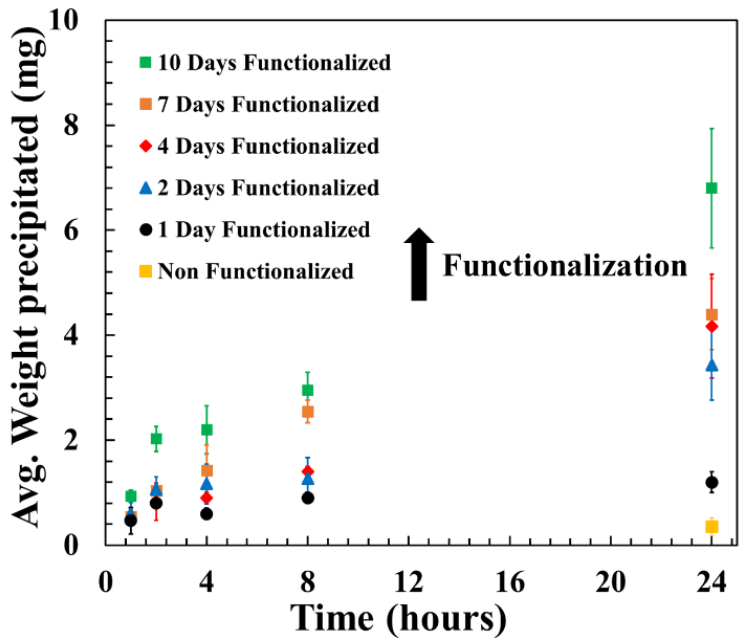


Figure 7: Weight based precipitation of calcite growth on surface functionalized 2D films.

To better understand how the surface energy (as characterized by contact angle) impacts calcite growth in general, a series of contact angle experiments and calcite precipitation experiments were performed using two other commercial polymeric materials poly(styrene-b-butadiene-b-styrene) (SBS) and poly(lactic acid) (PLA). Films of SBS and PLA were prepared, their contact angle measured, and analogous calcite precipitation experiments (SI = 3.15) were performed (**Fig. 8**). As shown in **Figure 8B**, SBS—due to its significant polystyrene content—exhibits a contact angle similar to that of HIPS, though slightly

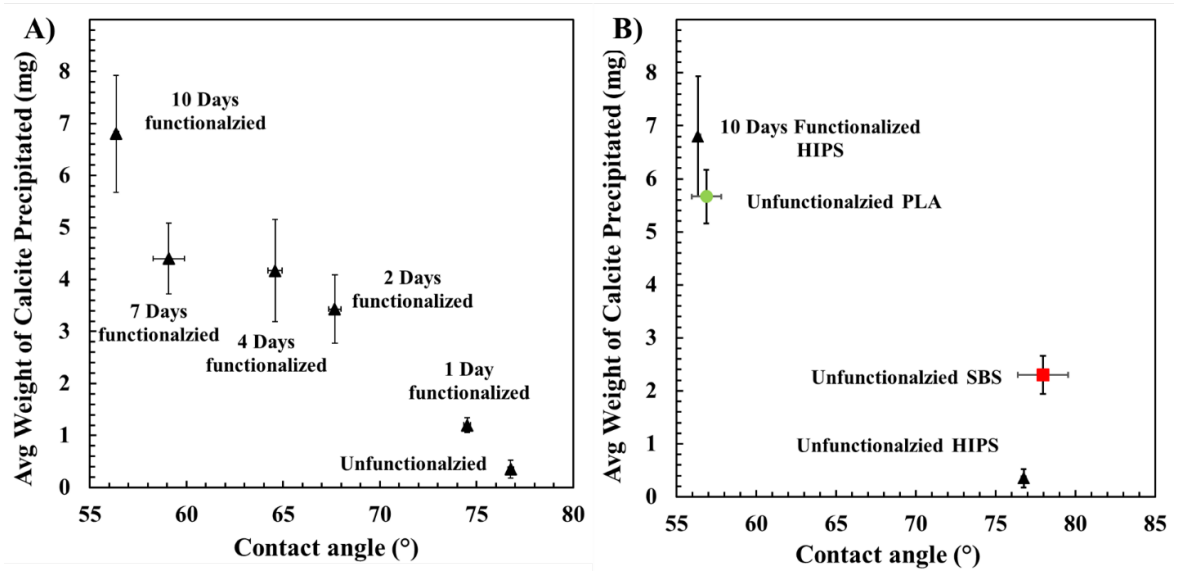


Figure 8: A) Average weight of calcite precipitated as a function of surface functionalization time, showing a corresponding decrease in contact angle of the functionalized HIPS films. **B)** Relationship between surface energy (represented by contact angle) and the average weight of calcite precipitated on unfunctionalized HIPS, SBS PLA, and functionalized HIPS films.

 https://doi.org/10.69631/ipj.v2i2nr71

higher on average. In contrast, PLA displays a lower contact angle, comparable to that of HIPS films functionalized for 10 days. Notably, the resulting amount of calcite precipitation is clearly tied to the contact angle as the amounts of calcite precipitate are similar for these pairs with similar contact angle; HIPS and SBS versus PLA and 10-day functionalized HIPS.

As noted in the introduction, the saturation index played a significant role in precipitation, with increased precipitation observed with increasing saturation indices (31, 41). To confirm this behavior here, and enable prediction of calcite precipitation for varied saturation indices on surface functionalized HIPS, calcite precipitation experiments were performed on the 10-day functionalized HIPS films for varying saturation indices (1.42, 2, 2.5, 2.72 and 3.15) for a precipitation time of 24 hours. While no precipitation was observed for the films with a SI of 2.0 after 24 hours, the amount of precipitation steadily increased with an increasing SI; **Table 2**.

Table 2: Weight based precipitation of calcite growth on surface functionalized 2D films (24 hours experiment) with varying saturation index.

Saturation Index	Average weight of calcite precipitated (mg)
1.42	No measurable precipitation
2.0	No measurable precipitation
2.5	1.63 ± 0.30
2.72	2.67 ± 0.15
3.15	6.83 ± 1.14

Given the promising results above for manipulating the precipitation of calcite on HIPS surfaces, four 3D printed HIPS cores were fabricated, of which two were then functionalized using sulfuric acid (F-1 and F-2) and two were left unfunctionalized (U-1 and U-2). These cores were then used in core-flooding calcite precipitation experiments and imaged using X-ray CT. The properties of the analyzed 3D X-ray micro-CT images are given in **Table 3**. A region of interest, 1.22 x 1.22 x 2.05 cm, was selected for each sample for consistency in the image analysis. The printed sample porosities, overall, are consistent: 29.0%, 31.2%, and 30.0% for U-1, F-1, and F-2, respectively (standard deviation of 0.9%). However, the porosity for U-2 is slightly larger than the others (33.5%). This is likely due to some printing defects within the complex heterogeneous pore structure. The unconnected porosity of the samples was also determined via analysis of the segmented images of the samples, which was ~0.4%, suggesting minimal inter-layer defects from the printing process.

Calcite precipitation is evident in 3D X-ray micro-CT images of the reacted samples (**Fig. 9**). In functionalized samples, analysis of the segmented images shows a uniform distribution of calcite precipitates throughout the entire sample. This corresponds to a decrease in post-experiment porosity throughout the samples. The volume fraction of calcite precipitated in the functionalized samples is approximately 2.6% which corresponds to a mass of approximately 0.21 g of calcite for the porous media volume of 3.05 cm^3. In contrast, only a small amount of calcite precipitation is evident in unfunctionalized samples, <1.1%, with a corresponding mass of approximately less than 0.09 g. As such, there are only

Table 3: Sample properties extracted from 3D X-ray micro-CT image of 3D-printed samples.

Printed sample	Properties	Functionalized Samples		Unfunctionalized Samples	
		F-1	F-2	U-1	U-2
Initial, unreacted sample	Connected porosity (%)	29.8	29.7	28.6	33.1
	Unconnected porosity (%)	0.4	0.3	0.4	0.4
	Total porosity (%)	31.2	30.0	29.0	33.5
Reacted sample	Calcite volume fraction (%)	2.6	2.5	1.1	0.6
	Final porosity (%)	28.6	27.5	27.9	32.9

 https://doi.org/10.69631/ipj.v2i2nr71

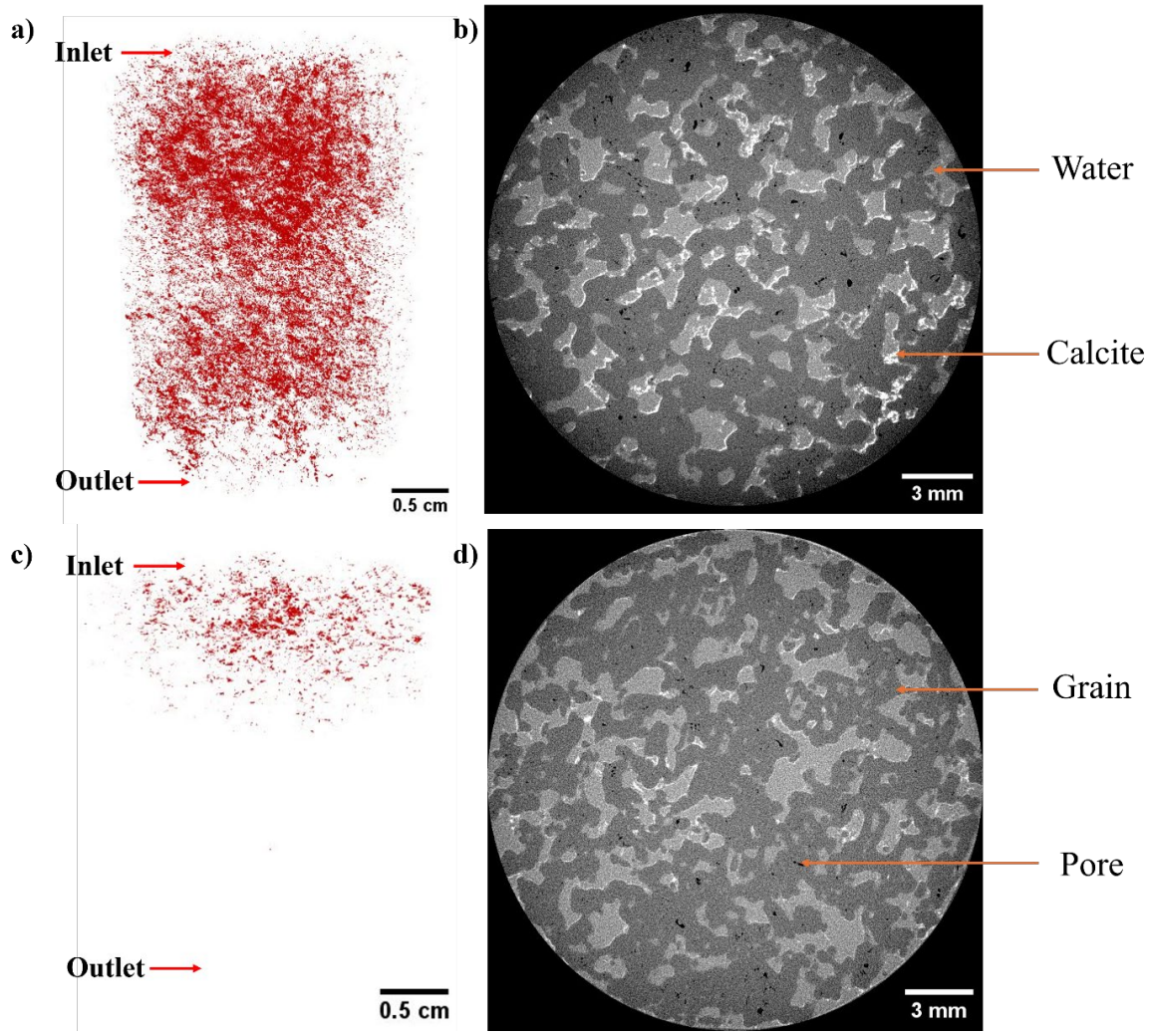


Figure 9: a) Calcite distribution in the functionalized sample (F-2), **b)** Reacted slice of functionalized sample (F-2), **c)** calcite distribution in unfunctionalized sample (U-2), and **d)** reacted slice of unfunctionalized sample (U-2).

small changes in porosity. The significant difference in calcite growth between functionalized and unfunctionalized samples demonstrates the importance of surface functionalization in promoting mineral precipitation. By manipulating the 3D printed porous media surface through functionalization, the precipitation of calcite within the porous media can be manipulated, and this is therefore a promising platform for geochemical reaction studies.

Figure 10 shows the calcite precipitation percentage in each slice of the 3D X-ray micro-CT images for all samples. Overall, greater extents of calcite precipitation are evident in functionalized samples as compared to unfunctionalized samples. Higher percentages of calcite precipitation can be found near the inlet for all samples. In the unfunctionalized samples, precipitation predominantly occurred near the inlet, with little precipitation throughout the rest of the sample. In the functionalized samples, the calcite precipitation was more uniform throughout the sample, albeit there were higher concentrations near the inlet, particularly for F-1.

Critically, the functionalized samples exhibited consistent and substantial calcite deposition within the porous media, indicating that surface functionalization not only enhances the reactivity of 3D-printed porous media, but also influences the spatial distribution of calcite precipitation. Notably, calcite precipitation in the functionalized porous media samples also reduces the porosity, suggesting this approach may be valuable in discerning changes in petrophysical properties, such as porosity evolution, that occur during reactions in porous media samples.

 https://doi.org/10.69631/ipj.v2i2nr71

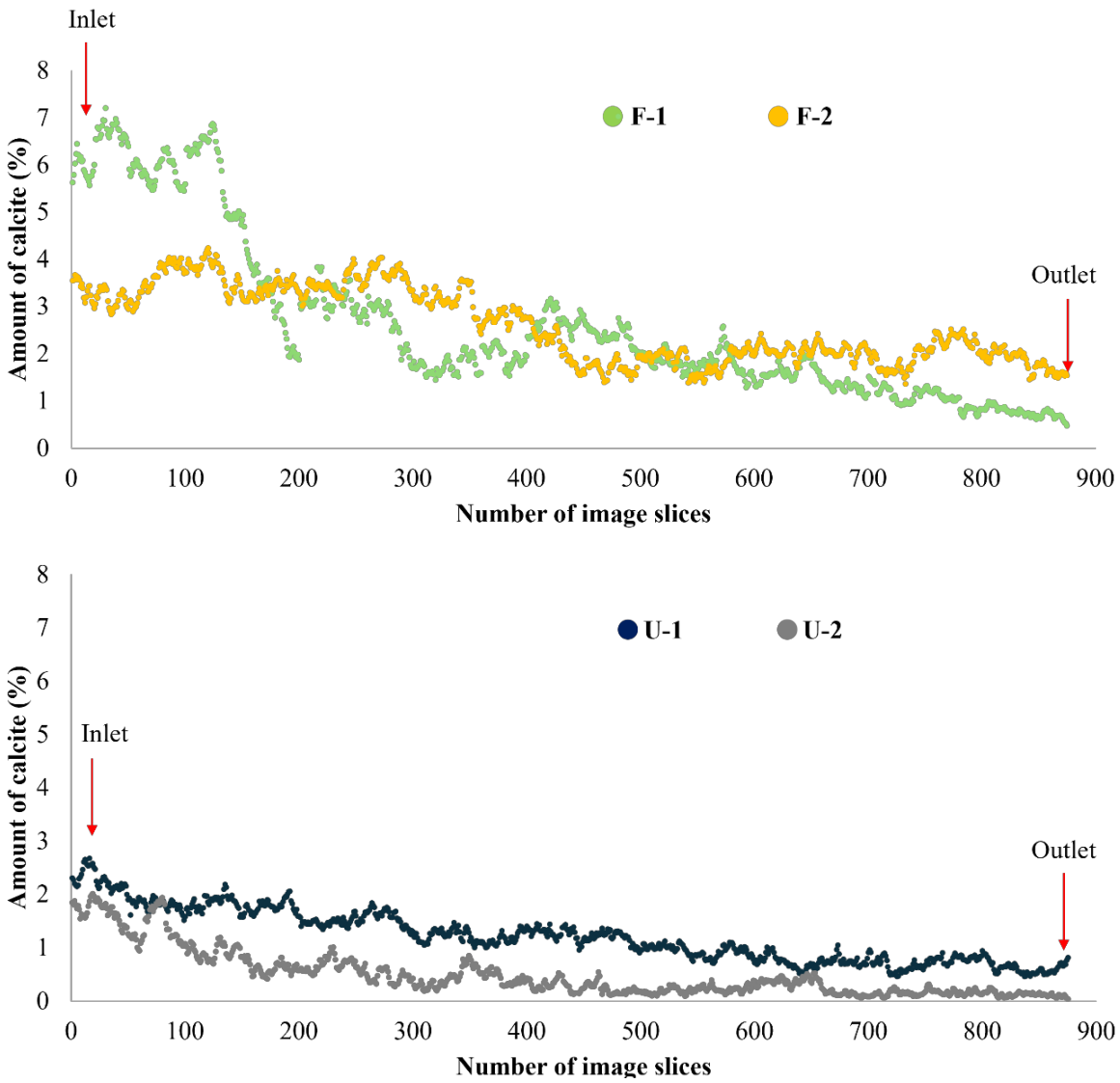


Figure 10: Percentage of calcite precipitation in each 3D X-ray micro-CT image slice of 3D-printed porous media for the functionalized samples F-1 and F-2 (top) and unfunctionalized samples U-1 and U-2 (bottom).

The successful use of functionalized 3D-printed porous media in these experiments underscores the potential of this approach for precisely manipulating pore structure and surface properties. Unlike natural rock samples, which often exhibit significant variability in composition and structure, 3D-printed functionalized media provide a more reproducible and systematic platform for studying mineral precipitation and reactive transport processes. Moreover, the proposed 3D printing method with functionalized material surfaces offers significant advantages over conventional 3D printing techniques by enabling targeted surface modifications without altering the bulk properties of the printed structures. Unlike traditional approaches that rely on mixing reactive particles within the material (54, 56), surface functionalization enhances mineral precipitation by directly modifying the chemical reactivity of the exposed surfaces. While calcite growth in a 2D film study demonstrates greater control over precipitation kinetics by functionalizing the surface area, functionalized 3D-printed porous media shows more uniform mineral growth in replicable experimental conditions in comparison to unfunctionalized 3D-printed porous media.

Functionalized 3D-printed porous media also have a unique application potential in CO_2 sequestration, groundwater remediation, geochemical modeling, and engineered biomineralization. This approach contributes to advancements in subsurface engineering, environmental sustainability, and mineral-based

material design by providing a scalable and customizable platform for studying reactive mechanisms and transport processes.

4. CONCLUSION

In this research, the surface functionalization of HIPS films and the impact of surface functionalization and saturation index on the calcite precipitation was first investigated. While FTIR and ^{1}H NMR spectroscopy confirms the partial surface functionalization of the HIPS films, there was no discernable surface degradation due to the acid treatment observed with optical microscopy or gravimetric analysis. Increasing the sulfonation time led to decreasing surface contact analysis and ultimately increased calcite precipitation in flow through precipitation experiments. From this, the hypothesis that the functionalization of the HIPS surface with sulfonic acid groups will promote the precipitation of calcite was confirmed. We attribute this phenomenon to the presence of sulfonic moieties which lower the surface energy facilitating the precipitation of calcite crystals by lowering the energy barrier for crystal nucleation and promoting crystal growth. More broadly, this surface functionalization approach has potential for enhancing the precipitation of other mineral phases or even preferential precipitation of mineral phases from solution onto polymer surfaces. Critically, this enabled the fabrication of replicate porous media using HIPS and filament-based 3D printing (fused filament fabrication) where the impact of surface functionalization on precipitation of calcite was then evaluated.

Core flooding experiments of unfunctionalized and functionalized 3D printed cores revealed significant calcite growth and porosity reduction in functionalized samples, while unfunctionalized samples showed little calcite precipitation and minimal porosity change. Three dimensional X-ray micro-CT imaging provided visual confirmation of these findings, highlighting the uniform distribution of calcite deposits in functionalized samples. Controlling pore structure and surface properties with 3D-printed porous media offers a potentially reproducible and systematic approach to studying geochemical reactions. The functionalization of these samples enhances their reactivity, enabling detailed investigations of mineral precipitation processes. The observed reduction in porosity due to calcite precipitation in functionalized samples suggests a promising way for elucidating the behavior of natural geochemical processes, underscoring the potential of 3D-printed media to mimic both the chemical and physical aspects of rock-fluid interactions.

The fabrication of such replicate porous media would enable better understanding of mineral precipitation and the impact of mineral precipitation on porosity and permeability, the focus of a future study. Beyond porous media, the ability to promote and control mineral precipitation is broadly important for other applications such as biomedical implants and water purification, and requires a better understanding of the structure property relationships between the polymer materials, solution character, and precipitation phenomena such as that investigated here.

The implications of this study are significant for geochemical modelling and experimentation. 3D-printed samples provide an effective and customizable platform for various applications, allowing researchers to tailor samples for specific reactions and conditions. This research paves the way for further exploration of 3D-printed porous media in various geochemical contexts, offering a promising tool for advancing our understanding of mineral reactions and other geochemical processes.

STATEMENTS AND DECLARATIONS

Supplementary Material

All supplementary or supporting information provided by the authors will be published online alongside the main article. When such material is available, it will also be indicated here along with a link to the pdf for downloading.

Author Contributions

Harrish Kumar Senthil Kumar: Conceptualization, Methodology, Formal analysis, Investigation, Data Curation, Visualization, Writing – Original Draft, Writing – Review & Editing. **Abdullah Al Nahian:** Data curation, Formal analysis, Investigation, Methodology, Software, Validation, Visualization, Writing – Original draft, Writing – Review & Editing. **Zhoufan Shi:** Methodology. **Nailah Braziel:** Investigation. **Madelyn Torrance:** Investigation. **Vinita V. Shinde:** Conceptualization, Methodology, Investigation, Writing – Review & Editing. **Lauren E. Beckingham:** Conceptualization, Methodology, Resources, Software, Writing – Review & Editing, Supervision, Project Administration, Funding Acquisition. **Bryan S. Beckingham:** Conceptualization, Methodology, Resources, Writing – Review & Editing, Supervision, Project Administration, Funding Acquisition.

Conflicts of Interest

There are no conflicts of interest to declare.

Data, Code & Protocol Availability

Data, codes, and protocol available from the authors upon request.

Funding Received

This material is based upon work supported by the National Science Foundation under Grant No. 2025626, Grant No. EEC-1950304, and by Auburn University.

ORCID IDs

Harrish Kumar Senthil Kumar https://orcid.org/0009-0003-4312-808X
Abdullah Al Nahian https://orcid.org/0000-0001-8368-8178
Nailah Braziel https://orcid.org/0009-0003-0628-0162
Zhoufan Shi https://orcid.org/0000-0001-6680-0906
Madelyn Torrance https://orcid.org/0009-0002-4568-930X
Vinita V. Shinde https://orcid.org/0000-0001-5079-7992
Lauren E. Beckingham https://orcid.org/0000-0002-8433-9532
Bryan S. Beckingham https://orcid.org/0000-0003-4004-0755

REFERENCES

1. Akella, S. V., Mowitz, A., Heymann, M., & Fraden, S. (2014). Emulsion-Based Technique To Measure Protein Crystal Nucleation Rates of Lysozyme. *Crystal Growth & Design*, 14(9), 4487-4509. https://doi.org/10.1021/cg500562r
2. Algive, L., Békri, S., Nader, F. H., Lerat, O., & Vizika, O. (2012). Impact of diagenetic alterations on the petrophysical and multiphase flow properties of carbonate rocks using a reactive pore network modeling approach. *Oil & Gas Science and Technology–Revue d'IFP Energies nouvelles*, 67(1), 147-160. http://dx.doi.org/10.2516/ogst/2011171
3. Al-Jaroudi, S. S., Ul-Hamid, A., Mohammed, A.-R. I., & Saner, S. (2007). Use of X-ray powder diffraction for quantitative analysis of carbonate rock reservoir samples. *Powder Technology*, 175(3), 115-121. https://doi.org/10.1016/j.powtec.2007.01.013
4. Al Nasser, W. N., & Al Salhi, F. H. (2015). Kinetics determination of calcium carbonate precipitation behavior by inline techniques. *Powder Technology*, 270, 548-560. https://doi.org/10.1016/j.powtec.2014.05.025
5. Al Nasser, W. N., Shaikh, A., Morriss, C., Hounslow, M. J., & Salman, A. D. (2008). Determining kinetics of calcium carbonate precipitation by inline technique. *Chemical Engineering Science*, 63(5), 1381-1389. https://doi.org/10.1016/j.ces.2007.07.051
6. Al Omari, M. M. H., Rashid, I. S., Qinna, N. A., Jaber, A. M., & Badwan, A. A. (2016). Calcium carbonate. In: *Profiles of Drug Substances, Excipients and Related Methodology* (Vol. 41, pp. 31–132). Elsevier. https://doi.org/10.1016/bs.podrm.2015.11.003
7. Al-Yaseri, A. Z., Roshan, H., Zhang, Y., Rahman, T., Lebedev, M., et al. (2017). Effect of the temperature on CO_2/brine/dolomite wettability: Hydrophilic versus hydrophobic surfaces. *Energy & Fuels*, 31(6), 6329-6333. https://doi.org/10.1021/acs.energyfuels.7b00745

8. Amos, R. T., Blowes, D. W., Bailey, B. L., Sego, D. C., Smith, L., & Ritchie, A. I. M. (2015). Waste-rock hydrogeology and geochemistry. *Applied Geochemistry*, 57, 140-156. https://doi.org/10.1016/j.apgeochem.2014.06.020
9. Anjikar, I. S., Wales, S., & Beckingham, L. E. (2020). Fused Filament Fabrication 3-D Printing of Reactive Porous Media. *Geophysical Research Letters*, 47(9), e2020GL087665. https://doi.org/10.1029/2020GL087665
10. Arns, C. H., Knackstedt, M. A., & Pinczewski, W. V. (2003). Effect of network topology on relative permeability. *Water Resources Research,* 39(12), 1285. http://dx.doi.org/10.11648/j.pse.20170201.15
11. Aschauer, U., Ebert, J., Aimable, A., & Bowen, P. (2010). Growth Modification of Seeded Calcite by Carboxylic Acid Oligomers and Polymers: Toward an Understanding of Complex Growth Mechanisms. *Crystal Growth & Design*, 10(9), 3956-3963. https://doi.org/10.1021/cg1005105
12. Atchley, A. L., Navarre-Sitchler, A. K., & Maxwell, R. M. (2014). The effects of physical and geochemical heterogeneities on hydro-geochemical transport and effective reaction rates. *Journal of Contaminant Hydrology,* 165, 53-64. https://doi.org/10.1016/j.jconhyd.2014.07.008
13. Babaei, M., & Joekar-Niasar, V. (2016). A transport phase diagram for pore-level correlated porous media. *Advances in Water Resources*, 92, 23-29. https://doi.org/10.1016/j.advwatres.2016.03.014
14. Bachu, S. (2000). Sequestration of CO_2 in geological media: criteria and approach for site selection in response to climate change. *Energy Conversion and Management*, 41(9), 953-970. https://doi.org/10.1016/S0196-8904(99)00149-1
15. Balashov, V. N., Guthrie, G. D., Hakala, J. A., Lopano, C. L., Rimstidt, J. D., & Brantley, S. L. (2013). Predictive modeling of CO2 sequestration in deep saline sandstone reservoirs: Impacts of geochemical kinetics. *Applied Geochemistry*, 30, 41-56. https://doi.org/10.1016/j.apgeochem.2012.08.016
16. Beckingham, L. E., Peters, C. A., Um, W., Jones, K. W., & Lindquist, W. B. (2013). 2D and 3D imaging resolution trade-offs in quantifying pore throats for prediction of permeability. *Advances in Water Resources*, 62, 1-12. https://doi.org/10.1016/j.advwatres.2013.08.010
17. Beckingham, L. E. (2017). Evaluation of macroscopic porosity–permeability relationships in heterogeneous mineral dissolution and precipitation scenarios. *Environmental Engineering Science*, 34(1), 64–73. https://doi.org/10.1002/2017WR021306
18. Bijeljic, B., Mostaghimi, P., & Blunt, M. J. (2011). Signature of non-Fickian solute transport in complex heterogeneous porous media. *Physical Review Letters*, 107(20), 204502. https://doi.org/10.1103/PhysRevLett.107.204502
19. Binsbergen, F. L. (1973). Heterogeneous nucleation of crystallization. *Progress in Solid State Chemistry*, 8, 189-238. https://doi.org/https://doi.org/10.1016/0079-6786(73)90007-1
20. Brantley, S. L., Holleran, M. E., Jin, L., & Bazilevskaya, E. (2013). Probing deep weathering in the Shale Hills Critical Zone Observatory, Pennsylvania (USA): the hypothesis of nested chemical reaction fronts in the subsurface. *Earth Surface Processes and Landforms*, 38(11), 1280-1298. https://doi.org/10.1002/esp.3415
21. Kralj, D., Kontrec, J., Brečević, L., Falini, G. and Nöthig-Laslo, V. (2004), Effect of Inorganic Anions on the Morphology and Structure of Magnesium Calcite. *Chemistry – A European Journal*, 10: 1647-1656. https://doi.org/10.1002/chem.200305313
22. Brookins, D. G. (2012). Geochemical Aspects of Radioactive Waste Disposal. Springer Science & Business Media. https://link.springer.com/book/10.1007/978-1-4613-8254-6
23. Bruderer, C., & Bernabé, Y. (2001). Network modeling of dispersion: Transition from Taylor dispersion in homogeneous networks to mechanical dispersion in very heterogeneous ones. *Water Resources Research*, 37(4), 897-908. https://doi.org/10.1029/2000WR900362
24. Buades, A., Coll, B., & Morel, J. M. (2011). Non-Local Means Denoising. *Image Processing On Line*, 1, 208-212. https://doi.org/10.5201/ipol.2011.bcm_nlm
25. Calhoun, A., & Chiang, E. (2006). Determination of the surface energetics of surface modified calcium carbonate using inverse gas chromatography. *Journal of Vinyl and Additive Technology*, 12(4), 174-182. https://doi.org/10.1002/vnl.20084
26. Chadha, R., Arora, P., Saini, A., & Bhandari, S. (2012). Crystal Forms of Anti-HIV Drugs: Role of Recrystallization. *Recrystallization*, 19, 447-464. http://dx.doi.org/10.5772/33777
27. Chang, R., Kim, S., Lee, S., Choi, S., Kim, M., & Park, Y. (2017). Calcium carbonate precipitation for CO2 storage and utilization: a review of the carbonate crystallization and polymorphism. *Frontiers in Energy Research*, 5, 17. https://doi.org/10.3389/fenrg.2017.00017
28. Chen, S. F., Zhu, J. H., Jiang, J., Cai, G. B., & Yu, S. H. (2010). Polymer-Controlled Crystallization of Unique Mineral Superstructures. Advanced Materials, 22(4), 540-545. https://doi.org/10.1002/adma.200901964
29. Cheong, W. C. (2010). Biomimetic approach to anti-fouling surfaces. (PhD Thesis) University of Leeds. https://etheses.whiterose.ac.uk/id/eprint/1694/

30. Crandell, L. E., Peters, C. A., Um, W., Jones, K. W., & Lindquist, W. B. (2012). Changes in the pore network structure of Hanford sediment after reaction with caustic tank wastes. *Journal of Contaminant Hydrology*, 131(1-4), 89-99. https://doi.org/10.1016/j.jconhyd.2012.02.002
31. De Choudens-Sanchez, V., & Gonzalez, L. A. (2009). Calcite and Aragonite Precipitation Under Controlled Instantaneous Supersaturation: Elucidating the Role of $CaCO_3$ Saturation State and Mg/Ca Ratio on Calcium Carbonate Polymorphism. *Journal of Sedimentary Research*, 79(6), 363-376. https://doi.org/10.2110/jsr.2009.043
32. Deng, Y., Harsh, J. B., Flury, M., Young, J. S., & Boyle, J. S. (2006). Mineral formation during simulated leaks of Hanford waste tanks. *Applied Geochemistry*, 21(8), 1392-1409. https://doi.org/10.1016/j.apgeochem.2006.05.002
33. Dentz, M., Cortis, A., Scher, H., & Berkowitz, B. (2004). Time behavior of solute transport in heterogeneous media: transition from anomalous to normal transport. *Advances in Water Resources*, 27(2), 155-173. https://doi.org/10.1016/j.advwatres.2003.11.002
34. Dentz, M., Hidalgo, J. J., & Lester, D. (2023). Mixing in porous media: concepts and approaches across scales. *Transport in Porous Media*, 146(1), 5-53. https://doi.org/10.1007/s11242-022-01852-x
35. DePaolo, D. J., & Cole, D. R. (2013). Geochemistry of geologic carbon sequestration: an overview. *Reviews in Mineralogy and Geochemistry*, 77(1), 1-14. https://doi.org/10.2138/rmg.2013.77.1
36. Esteves, L., Younes, A., Zeng, Y., & Dizier, A. (2020). Pore-network modeling of single-phase reactive transport in carbonates: Acidizing efficiency and wormholing regimes. *Chemical Engineering Journal,* 382, 122860. https://doi.org/10.1016/j.advwatres.2020.103741
37. Fahim Salek, M., Shinde, V. V., Beckingham, B. S., & Beckingham, L. E. (2022). Resin based 3D printing for fabricating reactive porous media. *Materials Letters*, 322, 132469. https://doi.org/10.1016/j.matlet.2022.132469
38. Flaten, E. M., Seiersten, M., & Andreassen, J.-P. (2010). Induction time studies of calcium carbonate in ethylene glycol and water. *Chemical Engineering Research and Design*, 88(12), 1659-1668. https://doi.org/10.1016/j.cherd.2010.01.028
39. Fowkes, F. M. (1964). Attractive forces at interfaces. *Industrial & Engineering Chemistry*, 56(12), 40-52. https://doi.org/10.1021/ie50660a008
40. Garside, J., Brečević, L., & Mullin, J. (1982). The effect of temperature on the precipitation of calcium oxalate. Journal of Crystal Growth, 57(2), 233-240. https://doi.org/10.1016/0022-0248(82)90478-X
41. Gebrehiwet, T. A., Redden, G. D., Fujita, Y., Beig, M. S., & Smith, R. W. (2012). The Effect of the CO_3^{2-} to Ca^{2+} Ion activity ratio on calcite precipitation kinetics and Sr^{2+} partitioning. *Geochemical Transactions*, 13, 1-11. https://doi.org/10.1186/1467-4866-13-1
42. Gibson, H. W., & Bailey, F. C. (1980). Chemical Modification of Polymers. 13. *Sulfonation of Polystyrene Surfaces. Macromolecules*, 13(1), 34-41. https://doi.org/10.1021/ma60073a007
43. Gibson, H. W., & Bailey, F. C. (1981). Chemical modification of polymers: 17. Dyeing of sulphonated polystyrene films by ion exchange with cationic dyes. *Polymer*, 22(8), 1068-1072. https://doi.org/10.1016/0032-3861(81)90294-9
44. Gould, R. F. (1964). Contact Angle, Wettability, and Adhesion, Copyright, Advances in Chemistry Series. In F. G. Robert (Ed.), *Contact Angle, Wettability, and Adhesion* (Vol. 43, pp. i-iii). American Chemical Society. https://doi.org/doi:10.1021/ba-1964-0043.fw001
45. Heller, W., Cheng, M.-H., & Greene, B. W. (1966). Surface tension measurements by means of the "microcone tensiometer". *Journal of Colloid and Interface Science*, 22(2), 179-194. https://doi.org/10.1016/0021-9797(66)90082-8
46. Hilley, G. E., & Porder, S. (2008). A framework for predicting global silicate weathering and CO_2 drawdown rates over geologic time-scales. *Proceedings of the National Academy of Sciences*, 105(44), 16855-16859. https://doi.org/10.1073/pnas.0801462105
47. Hoefner, M. L., & Fogler, H. S. (1988). Pore evolution and channel formation during flow and reaction in porous media. *AIChE Journal*, 34(1), 45–54. https://doi.org/10.1002/aic.690340107
48. Hua, K.-H., Wang, H.-C., Chung, R.-S., & Hsu, J.-C. (2015). Calcium carbonate nanoparticles can enhance plant nutrition and insect pest tolerance. *Journal of Pesticide Science*, 40(4), 208-213. https://doi.org/10.1584/jpestics.D15-025
49. Hussein, A. (2022). *Essentials of Flow Assurance Solids in Oil and Gas Operations: Understanding Fundamentals, Characterization, Prediction, Environmental Safety, and Management*. Gulf Professional Publishing. https://doi.org/10.1016/C2021-0-00361-8
50. Jaho, S., Sygouni, V., Rokidi, S. G., Parthenios, J., Koutsoukos, P. G., & Paraskeva, C. A. (2016). Precipitation of Calcium Carbonate in Porous Media in the Presence of n-Dodecane. *Crystal Growth & Design,* 16(12), 6874-6884. https://doi.org/10.1021/acs.cgd.6b01048

51. Jones, A. G. (2002). *Crystallization Process Systems*. Elsevier. 978-0-7506-5520-0. https://www.sciencedirect.com/book/9780750655200/crystallization-process-systems#book-info
52. Khather, M., Saeedi, A., Rezaee, R., Noble, R. R., & Gray, D. (2017). Experimental investigation of changes in petrophysical properties during CO_2 injection into dolomite-rich rocks. *International Journal of Greenhouse Gas Control*, 59, 74-90. https://doi.org/10.1016/j.ijggc.2017.02.007
53. Kim, Y., Seol, Y., Lee, H., & Kneafsey, T. (2011). Upscaling geochemical reaction rates accompanying acidic CO_2-saturated brine flow in sandstone. *Water Resources Research*, 47, W06506. https://doi.org/10.1029/2010WR009472
54. Kong, L., Ostadhassan, M., Li, C., & Tamimi, N. (2018). Can 3-D printed gypsum samples replicate natural rocks? An experimental study. *Rock Mechanics and Rock Engineering*, 51, 3061-3074. https://doi.org/10.1007/s00603-018-1520-3
55. Kong, L., Ostadhassan, M., Hou, X., Mann, M., & Li, C. (2019). Microstructure characteristics and fractal analysis of 3D-printed sandstone using micro-CT and SEM-EDS. *Journal of Petroleum Science and Engineering*, 175, 1039-1048. https://doi.org/10.1016/j.petrol.2019.01.050
56. Kong, L., Ishutov, S., Hasiuk, F., & Xu, C. (2021). 3D printing for experiments in petrophysics, rock physics, and rock mechanics: a review. *SPE Reservoir Evaluation & Engineering*, 24(04), 721-732. https://doi.org/10.2118/206744-PA
57. Lee, D., Ruf, M., Karadimitriou, N., Steeb, H., Manousidaki, M., et al. (2024). Development of stochastically reconstructed 3D porous media micromodels using additive manufacturing: numerical and experimental validation. *Scientific Reports*, 14(1), 9375. https://doi.org/10.1038/s41598-024-60075-w
58. Li, L., Peters, C. A., & Celia, M. A. (2006). Upscaling geochemical reaction rates using pore-scale network modeling. *Advances in Water Resources*, 29(9), 1351–1370. https://doi.org/10.1016/j.advwatres.2005.10.011
59. Li, L., Peters, C. A., & Celia, M. A. (2007). Effects of mineral spatial distribution on reaction rates in porous media. *Water Resources Research*, 43(1), W01419. https://doi.org/10.1029/2005WR004848
60. Lioliou, M. G., Paraskeva, C. A., Koutsoukos, P. G., & Payatakes, A. C. (2007). Heterogeneous nucleation and growth of calcium carbonate on calcite and quartz. *Journal of Colloid and Interface Science*, 308(2), 421-428. https://doi.org/10.1016/j.jcis.2006.12.045
61. Liu, C., Liu, Y., Kerisit, S., & Zachara, J. (2015). Pore-scale process coupling and effective surface reaction rates in heterogeneous subsurface materials. *Reviews in Mineralogy and Geochemistry,* 80(1), 191-216. https://doi.org/10.2138/rmg.2015.80.06
62. Liu, Y., Gong, W., Xiao, H., & Wang, M. (2024). A pore-scale numerical framework for solute transport and dispersion in porous media. *Advances in Water Resources*, 183, 104602. http://dx.doi.org/10.1016/j.advwatres.2023.104602
63. Liu, Y., Xiao, H., Aquino, T., Dentz, M., & Wang, M. (2024). Scaling laws and mechanisms of hydrodynamic dispersion in porous media. *Journal of Fluid Mechanics*, 1001, R2. http://dx.doi.org/10.1017/jfm.2024.1131
64. Luhmann, A. J., Tutolo, B. M., Bagley, B. C., Mildner, D. F., Seyfried Jr, et al. (2017). Permeability, porosity, and mineral surface area changes in basalt cores induced by reactive transport of CO_2-rich brine. *Water Resources Research*, 53(3), 1908-1927. https://doi.org/10.1002/2016WR019216
65. Ma, G., Zheng, Z., Wang, H., Wang, L., Zhao, G., et al. (2023). Effect of solution supersaturation on crystal formation of Vitamin K2 based on near infrared spectroscopy analysis technology. *Journal of Crystal Growth*, 605, 127034. https://doi.org/10.1016/j.jcrysgro.2022.127034
66. Ma, Y., Gao, Y., & Feng, Q. (2010). Effects of pH and temperature on $CaCO_3$ crystallization in aqueous solution with water soluble matrix of pearls. *Journal of Crystal Growth*, 312(21), 3165-3170. https://doi.org/10.1016/j.jcrysgro.2010.07.053
67. Maher, K. (2010). The dependence of chemical weathering rates on fluid residence time. *Earth and Planetary Science Letters*, 294(1-2), 101-110. https://doi.org/10.1016/j.epsl.2010.03.010
68. Maiwa, K., Nakamura, H., Kimura, H., & Miyazaki, A. (2006). Effect of temperature and supersaturation on the growth of Sr (No3) 2 (1 1 1) face in aqueous solution. *Journal of Crystal Growth*, 289(1), 303-307. https://doi.org/10.1016/j.jcrysgro.2005.10.110
69. Min, T., Gao, Y., Chen, L., Kang, Q., & Tao, W. W. (2016). Changes in porosity, permeability and surface area during rock dissolution: Effects of mineralogical heterogeneity. *International Journal of Heat and Mass Transfer*, 103, 900-913. https://doi.org/10.1016/j.ijheatmasstransfer.2016.07.043
70. Molins, S., Trebotich, D., Yang, L., Ajo-Franklin, J. B., Ligocki, T. J., et al. (2014). Pore-scale controls on calcite dissolution rates from flow-through laboratory and numerical experiments. *Environmental Science & Technology*, 48(13), 7453-7460. https://doi.org/10.1021/es5013438
71. Mullin, J. W. (2001). *Crystallization*. 4th Edition. Elsevier. https://doi.org/10.1016/B978-0-7506-4833-2.X5000-1
72. Murphy, W. L., & Mooney, D. J. (2002). Bioinspired growth of crystalline carbonate apatite on biodegradable polymer substrata. *Journal of the American Chemical Society*, 124(9), 1910-1917. https://doi.org/10.1021/ja012433n

73. Navarre-Sitchler, A., & Jung, H. (2017). Complex coupling of fluid transport and geochemical reaction rates: Insights from reactive transport models. *Procedia Earth and Planetary Science*, 17, 5-8. https://doi.org/10.1016/j.proeps.2016.12.004
74. Navarre-Sitchler, A. K., Cole, D. R., Rother, G., Jin, L., Buss, H. L., & Brantley, S. L. (2013). Porosity and surface area evolution during weathering of two igneous rocks. *Geochimica et Cosmochimica Acta*, 109, 400-413. https://doi.org/10.1016/j.gca.2013.02.012
75. Nicoleau, L., Van Driessche, A. E., & Kellermeier, M. (2019). A kinetic analysis of the role of polymers in mineral nucleation. The example of gypsum. *Cement and Concrete Research*, 124, 105837. https://doi.org/10.1016/j.cemconres.2019.105837
76. Nogues, J. P., Fitts, J. P., Celia, M. A., & Peters, C. A. (2013). Permeability evolution due to dissolution and precipitation of carbonates using reactive transport modeling in pore networks. *Water Resources Research*, 49(9), 6006-6021. https://doi.org/10.1002/wrcr.20486
77. Noiriel, C., Steefel, C. I., Yang, L., & Bernard, D. (2016). Effects of pore-scale precipitation on permeability and flow. *Advances in Water Resources*, 95, 125-137. https://doi.org/10.1016/j.advwatres.2015.11.013
78. Oskolkov, A. A., Kochnev, A. A., Krivoshchekov, S. N., & Savitsky, Y. V. (2024). Real-Size Reconstruction of Porous Media Using the Example of Fused Filament Fabrication 3D-Printed Rock Analogues. *Journal of Manufacturing and Materials Processing*, 8(3), 104. https://doi.org/10.3390/jmmp8030104
79. Parry, S. A., Hodson, M. E., Kemp, S. J., & Oelkers, E. H. (2015). The surface area and reactivity of granitic soils: I. Dissolution rates of primary minerals as a function of depth and age deduced from field observations. *Geoderma*, 237, 21-35. https://doi.org/10.1016/j.geoderma.2014.08.004
80. Raoof, A., Hassanizadeh, S. M., & Leijnse, A. (2010). Upscaling transport of adsorbing solutes in porous media: Pore-network modeling. *Vadose Zone Journal*, 9(1), 208–219. https://doi.org/10.2136/vzj2010.0026
81. Reis, R., Cunha, A., Fernandes, M., & Correia, R. (1997). Treatments to induce the nucleation and growth of apatite-like layers on polymeric surfaces and foams. *Journal of Materials Science: Materials in Medicine*, 8, 897-905. https://doi.org/10.1023/A:1018514107669
82. Roded, R., Szymczak, P., & Holtzman, R. (2021). Wormholing in anisotropic media: Pore-scale effect on large-scale patterns. *Geophysical Research Letters,* 48(11), e2021GL093659. http://dx.doi.org/10.1029/2021GL093659
83. Sahimi, M. U. H. A. M. M. A. D., & Imdakm, A. O. (1988). The effect of morphological disorder on hydrodynamic dispersion in flow through porous media. *Journal of Physics A: Mathematical and General,* 21(19), 3833. https://doi.org/10.1088/0305-4470/21/19/019
84. Sabo, M., & Beckingham, L. E. (2021). Porosity-permeability evolution during simultaneous mineral dissolution and precipitation: The impact of size-dependent reactivity. *Water Resources Research*, 57(9), e2021WR030261. https://doi.org/10.1029/2020WR029072
85. Salek, M. F., Shinde, V. V., Beckingham, B. S., & Beckingham, L. E. (2022). Resin based 3D printing for fabricating reactive porous media. *Materials Letters*, 322, 132469. https://doi.org/10.1016/j.matlet.2022.132469
86. Shinde, V. V., Wang, Y., Salek, M. F., Auad, M. L., Beckingham, L. E., & Beckingham, B. S. (2022). Material design for enhancing properties of 3D printed polymer composites for target applications. *Technologies*, 10(2), 45. https://doi.org/10.3390/technologies10020045
87. Shinde, V. V. (2022). Building a Sustainable Future through the Material design of 3D Printed Polymer Materials. Dissertation, Auburn University. https://etd.auburn.edu//handle/10415/8229
88. Song, R., Wang, Y., Sun, S., & Liu, J. (2021). Characterization and microfabrication of natural porous rocks: From micro-CT imaging and digital rock modelling to micro-3D-printed rock analogs. J*ournal of Petroleum Science and Engineering*, 205, 108827. https://doi.org/10.1016/j.petrol.2021.108827
89. Steinwinder, T. R., & Beckingham, L. E. (2019). Role of pore and pore-throat distributions in controlling permeability in heterogeneous mineral dissolution and precipitation scenarios. *Water Resources Research*, 55(9), 7417–7432. https://doi.org/10.1029/2019WR024793
90. Sugimoto, T. (2019). *Monodispersed Particles*. Elsevier. Paperback ISBN: 9780444546456, Hardback ISBN: 9780444895691, eBook ISBN: 9780080536965 https://shop.elsevier.com/books/monodispersed-particles/sugimoto/978-0-444-89569-1
91. Tang, H., Yu, J., & Zhao, X. (2009). Controlled synthesis of crystalline calcium carbonate aggregates with unusual morphologies involving the phase transformation from amorphous calcium carbonate. *Materials Research Bulletin,* 44(4), 831-835. https://doi.org/10.1016/j.materresbull.2008.09.002
92. Temmel, E., Gänsch, J., Seidel-Morgenstern, A., & Lorenz, H. (2020). Systematic investigations on continuous fluidized bed crystallization for chiral separation. *Crystals*, 10(5), 394. http://dx.doi.org/10.3390/cryst10050394
93. Trebotich, D., & Graves, D. T. (2015). An adaptive finite volume method for incompressible viscous flow in complex geometries. *Journal of Computational Physics*, 297, 155–172. https://doi.org/10.1006/jcph.2002.7037
94. Walles, W. (1973). Lamination of olefin polymer to various substrates. US Patent US3779840A.

95. Watt, J. C. (1925). The deposition of calcium phosphate and calcium carbonate in bone and in areas of calcification. *Archives of Surgery*, 10(3), 983-990.
96. Wen, H., & Li, L. (2017). An upscaled rate law for magnesite dissolution in heterogeneous porous media. *Geochimica et Cosmochimica Acta*, 210, 289-305. https://doi.org/10.1016/j.gca.2017.04.019
97. Varloteaux, C., Bekri, S., Vizika, O., & Noiriel, C. (2013). Pore network modelling to determine the transport properties of a real porous medium. *Advances in Water Resources*, 53, 121–131. https://doi.org/10.1016/j.advwatres.2012.10.004
98. Yang, J., Zhu, P., Xu, W., & Ma, S. (2022). Study on abrasive grinding characteristics of calcite. 2022 International Conference on Optoelectronic Information and Functional Materials. *Proceedings Volume 12255, 2022 International Conference on Optoelectronic Information and Functional Materials (OIFM 2022)*; 122551O (2022) https://doi.org/10.1117/12.2638722
99. Yang, L., Xu, T., Yang, B., Tian, H., & Lei, H. (2014). Effects of mineral composition and heterogeneity on the reservoir quality evolution with CO_2 intrusion. *Geochemistry, Geophysics, Geosystems*, 15(3), 605-618. https://doi.org/10.1002/2013GC005157
100. Yu, Z., Wang, J.-J., Liu, L.-Y., Li, Z., & Zeng, E. Y. (2024). Drinking boiled tap water reduces human intake of nanoplastics and microplastics. *Environmental Science & Technology Letters*, 11(3), 273-279. https://doi.org/10.1021/acs.estlett.4c00081
101. Zhang, L., Xu, C., Guo, Y., Zhu, G., Cai, S., et al. (2021). The effect of surface roughness on immiscible displacement using pore scale simulation. *Transport in Porous Media*, 140, 713-725. https://link.springer.com/article/10.1007/s11242-020-01526-6
102. Zhang, S., & DePaolo, D. J. (2017). Rates of CO_2 mineralization in geological carbon storage. Accounts of Chemical Research, 50(9), 2075-2084. https://doi.org/10.1021/acs.accounts.7b00334